

Article

# Hot Deformation Behavior of As-Cast and Homogenized $\text{Al}_{0.5}\text{CoCrFeNi}$ High Entropy Alloys

Yu Zhang, Jinshan Li \*, Jun Wang \*, Sizhe Niu and Hongchao Kou

State Key Laboratory of solidification processing, Northwestern Polytechnical University, NO.127, West Youyi Road, Xi'an 710072, China; zhangyu0113@126.com (Y.Z.); 15529396180@163.com (S.N.); hchkou@nwpu.edu.cn (H.K.)

\* Correspondence: ljsh@nwpu.edu.cn (J.L.); nwpuwj@nwpu.edu.cn (J.W.); Tel.: +86-29-8846-0568 (J.L. & J.W.); Fax: +86-29-8846-0294 (J.L. & J.W.)

Academic Editor: Michael C. Gao

Received: 10 September 2016; Accepted: 4 November 2016; Published: 15 November 2016

**Abstract:** The hot deformation behavior of as-cast and homogenized  $\text{Al}_{0.5}\text{CoCrFeNi}$  high entropy alloys (HEAs) during isothermal compression was investigated as a function of temperature and strain rate. Results indicated that flow stress in a homogenized state was always higher than that in an as-cast state under the same deformation conditions. Moreover, the optimum thermo-mechanical processing (TMP) conditions for the hot working of the homogenized state were identified as 945–965 °C and  $10^{-1.7}$ – $10^{-1.1}$  s<sup>-1</sup> and were easier to determine in practice. Constitutive equations, for both states, correlating the flow stress of  $\text{Al}_{0.5}\text{CoCrFeNi}$  with strain rate and deformation temperature were also determined.

**Keywords:** high entropy alloy; homogenization; flow stress; constitutive equation; processing map

## 1. Introduction

Multi-component high entropy alloys (HEAs), introduced by Yeh et al. as a new alloy exploration strategy, normally contain five or more principal alloying elements in equiatomic or a near-equiatomic ratios [1–4]. Research shows that a high mixing entropy caused by multiple principal components can inhibit the formation of intermetallic compounds and promote the formation of simple solid solution structures [3]. Moreover, through the composition optimization, HEAs possess high hardness, high strength, high temperature creep resistance, and other excellent properties [5–8], which have shown great potential both in theory research and application.

Previous research of HEAs has been focused on how element content influences the property and the microstructure evolution during different heat treatments. However, hot deformation behavior is less understood. As we all know, wrought alloys are more popular in engineering component production compared with cast alloys because of factors such as shrinkage porosity, coarse dendritic structure, chemical heterogeneity, and metastable eutectic at the grain boundaries [9]. A common metallurgical approach to solve these problems is thermo-mechanical processing (TMP) of the cast alloys.

$\text{Al}_x\text{CoCrFeNi}$  is a typical HEA system that possesses face centered cubic (FCC) ( $\text{Al}_0$ – $\text{Al}_{0.3}$ ), FCC + body centered cubic (BCC) ( $\text{Al}_{0.5}$ – $\text{Al}_{0.7}$ ), and BCC ( $\text{Al}_{0.9}$ – $\text{Al}_{1.8}$ ) structures with an increasing atom percent of Al [10–12]. Generally, the FCC-typed HEAs are soft and ductile [12–16], whereas the BCC-typed HEAs are hard and brittle [13–15,17]. As a two-phase alloy, the  $\text{Al}_{0.5}\text{CoCrFeNi}$  HEA has high plasticity and high strength, which gives it a more brilliant prospect than pure FCC or BCC alloys. However, there lies a dendritic microstructure with some segregation in dendrite (DR) and interdendrite (ID) regions in as-cast  $\text{Al}_x\text{CoCrFeNi}$  HEA ingots [18], resulting in a necessity of homogenizing before hot working. Therefore, in this paper, we select as-cast and homogenized

Al<sub>0.5</sub>CoCrFeNi as a research subject and obtain constitutive equations and processing maps by means of isothermal compression testing. The objective of this investigation was to identify the optimum TMP conditions and explore the influence of homogenization on the hot working of this alloy.

## 2. Materials and Methods

High purity Al, Co, Cr, Fe, and Ni ( $\geq 99.9\%$ ) were used as the raw material. Before charging into the crucible, all the alloying elements were cleaned with acetone and dried. The multicomponent Al, Co, Cr, Fe, and Ni was synthesized via arc melting under ultra-high purity argon gas on a water-cooled copper crucible to obtain an arc melted alloy button, each weighing about 30 g. To ensure chemical homogeneity, each button was flipped over and re-melted at least 5 times. The actual chemical composition was measured as 6.07 wt % Al, 23.95 wt % Co, 20.75 wt % Cr, 23.15 wt % Fe, and 24.26 wt % Ni, agreeing quite well with the nominal composition (5.65 wt % Al, 24.66 wt % Co, 21.76 wt % Cr, 23.37 wt % Fe, 24.56 wt % Ni) of Al<sub>0.5</sub>CoCrFeNi. Subsequently, button ingots were suction-casted in a water-cooled split Cu mold and cut into cylindrical samples that were 12 mm in length and 8 mm in diameter. Half of the samples were homogenized at 1100 °C for 20 h in a vacuum heat treating furnace and furnace-cooled, referring to a regime used previously for CoCrFeNi and CoCrFeMnNi [19,20]. The phase identification of both state samples was examined via DX 2700 X-ray diffraction (XRD, Dandong Fangyuan Instrument Co., Ltd., Dandong, China) with Cu-K $\alpha$  ( $\lambda = 0.154056$  nm) radiation, operating at 40 kV and 30 mA. Microstructure and compositional analyses were studied with a Zeiss Super 55 scanning electron microscope (SEM, Carl Zeiss AG, Oberkochen, Germany) equipped with an energy-dispersive spectrometer (EDS). Samples were carefully mechanically polished and then electropolished in a mixture of 90% acetic and 10% perchloric acids at room temperature and an applied voltage of 25 V for 15 s. The micrographs were obtained in the backscattered electron (BSE) imaging mode to reveal the different phases in the microstructure due to the atomic number (Z) contrast.

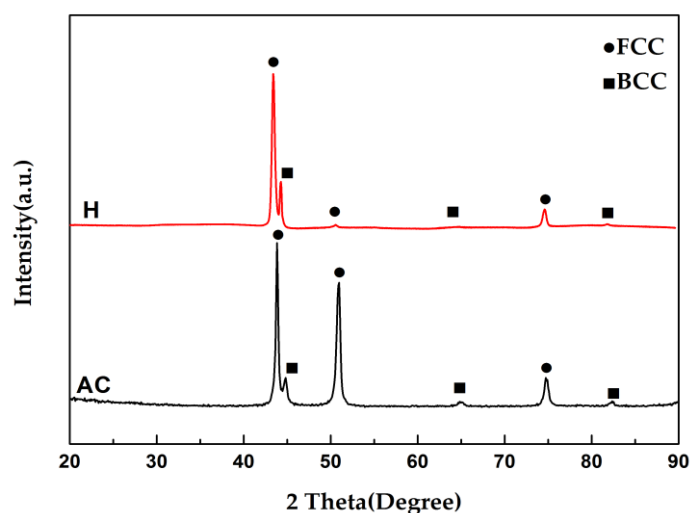
Isothermal hot compression tests were performed on cylindrical samples with dimensions of  $\Phi 8 \times 12$  mm using a Gleeble 3500 thermo-mechanical simulator (DSI, St. Paul, Poestenkill, NY, USA) at different deformation temperatures of 850, 900, 950, and 1000 °C with strain rates of 1,  $10^{-1}$ ,  $10^{-2}$ , and  $10^{-3}$  s $^{-1}$ . In order to ensure the reliability and repeatability of the experimental data, each test under the same deformation parameter was repeated at least three times. A graphite sheet was placed between the sample ends and anvil to ensure sufficient lubrication during each test. The samples were heated at a heating rate of 10 K/s from room temperature to the deformation temperature and kept for 180 s to eliminate the temperature gradient of the samples. Afterwards, they were deformed to a 60% reduction in height that corresponds to a true strain of  $\epsilon \sim 0.9$  and quenched with distilled water to freeze the microstructure. All tests were conducted in an argon atmosphere. During the process of compression, the temperature of the samples was measured by a thermocouple (nickel–chromium and nickel–silicon, Shanghai Feilong Meters & Electronics Co. Ltd, Shanghai, China) welded in the middle of the samples, and the flow stress was recorded as a function of the true strain for each strain rate and deformation temperature.

## 3. Results and Discussion

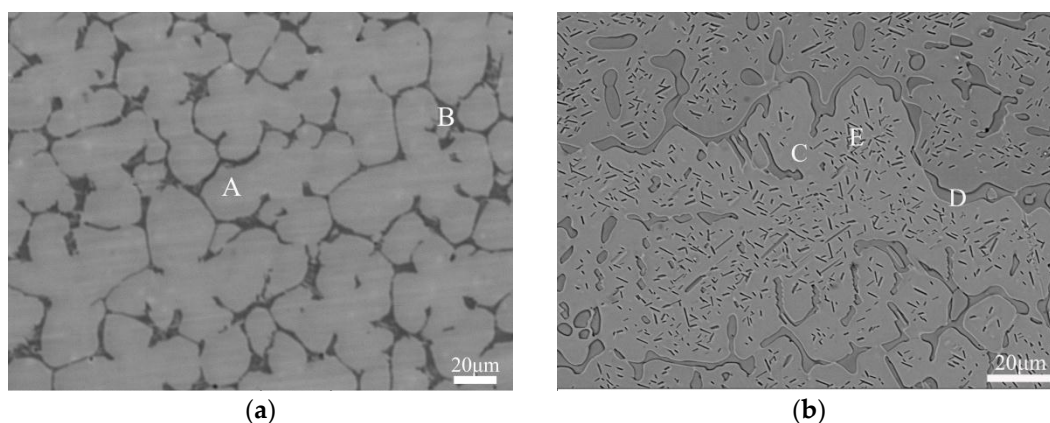
### 3.1. Microstructures

Figure 1 shows the XRD patterns of the as-cast and homogenized Al<sub>0.5</sub>CoCrFeNi HEAs. Both states exhibit a mixture of FCC and BCC crystalline structure, and the FCC phase is in majority according to the relative intensity of the diffraction peaks. After homogenization, the FCC peak intensity decreased while the BCC peak intensity increased, indicating that some FCC phases had transformed to a BCC phase. Figure 2 shows the microstructure of as-cast and homogenized specimens, and the chemical compositions of different phases are listed in Table 1. In Figure 2a, the as-cast alloy illustrates typical DR and ID regions, and the volume fraction of DR is 82%. Therefore, it is obvious

that the DR corresponds to the FCC phases, whereas the ID corresponds to the BCC phases. Besides, Al and Ni segregate to the ID in the as-cast alloy. This can be explained by the fact that Al has a relatively larger atom radius and that Al–Ni has a higher negative mixing enthalpy than other atom pairs among the five elements [21]. After homogenization, some of the ID regions redissolved into the matrix since they transformed from a continuous net-shaped phase to a separated droplet-shaped phase. Moreover, a large amount of acicular precipitation (P) rich in Al and Ni separated from the matrix. The volume fraction of the DR, the ID, and the P is 76%, 15% and 9%, respectively.



**Figure 1.** X-ray diffraction (XRD) patterns of as-cast and homogenized  $\text{Al}_{0.5}\text{CoCrFe}$  HEAs (AC stands for as-cast; H stands for homogenized).



**Figure 2.** Initial microstructure of the (a) as-cast and (b) homogenized  $\text{Al}_{0.5}\text{CoCrFeNi}$  HEAs. A, B, C, D and E correspond to different phases (A—DR, B—ID, C—DR, D—ID, E—P).

**Table 1.** The nominal composition and actual chemical compositions (in atom %) of different phases of the  $\text{Al}_{0.5}\text{CoCrFeNi}$  HEAs.

Elements		Al	Co	Cr	Fe	Ni
Nominal		11.12	22.22	22.22	22.22	22.22
As-cast	DR(A)	12.35	22.38	23.03	22.48	19.76
	ID(B)	22.24	17.52	18.02	18.01	24.21
Homogenized	DR(C)	8.95	21.74	25.77	24.62	18.92
	ID(D)	14.50	22.97	19.81	22.08	20.64
	P(E)	18.89	20.07	16.81	19.23	25.00

### 3.2. Flow Stress Behavior

The thermal expansion curve and its differential curve of the as-cast  $\text{Al}_{0.5}\text{CoCrFeNi}$  HEA are listed in Figure S1 in Supplementary Materials. Minimum points at 580 and 840 °C in the differential curve indicate the presence of a solid phase transformation. In other words, no solid state phase transformation took place at the deformation temperature (850–1000 °C) in this work. Figure 3 shows the true stress ( $\sigma$ )–true strain ( $\epsilon$ ) curves of the as-cast and homogenized  $\text{Al}_{0.5}\text{CoCrFeNi}$  HEAs at 900 and 1000 °C with strain rates of  $10^{-3}$ – $1 \cdot \text{s}^{-1}$ . At a fixed strain, flow stress increased with a decrease in deformation temperature and an increase in strain rate. It is evident from Figure 3 that the flow stress increased dramatically to a peak value with a relatively slight strain at an early stage followed by a softening until to the maximum strain. This is because hot deformation is a competing process between working hardening and dynamic softening [22,23]. Increasing deformation temperature will speed up the thermal activation process; however, increasing strain rate will accelerate the generation and multiplication of dislocation and make it more difficult to increase deformation.

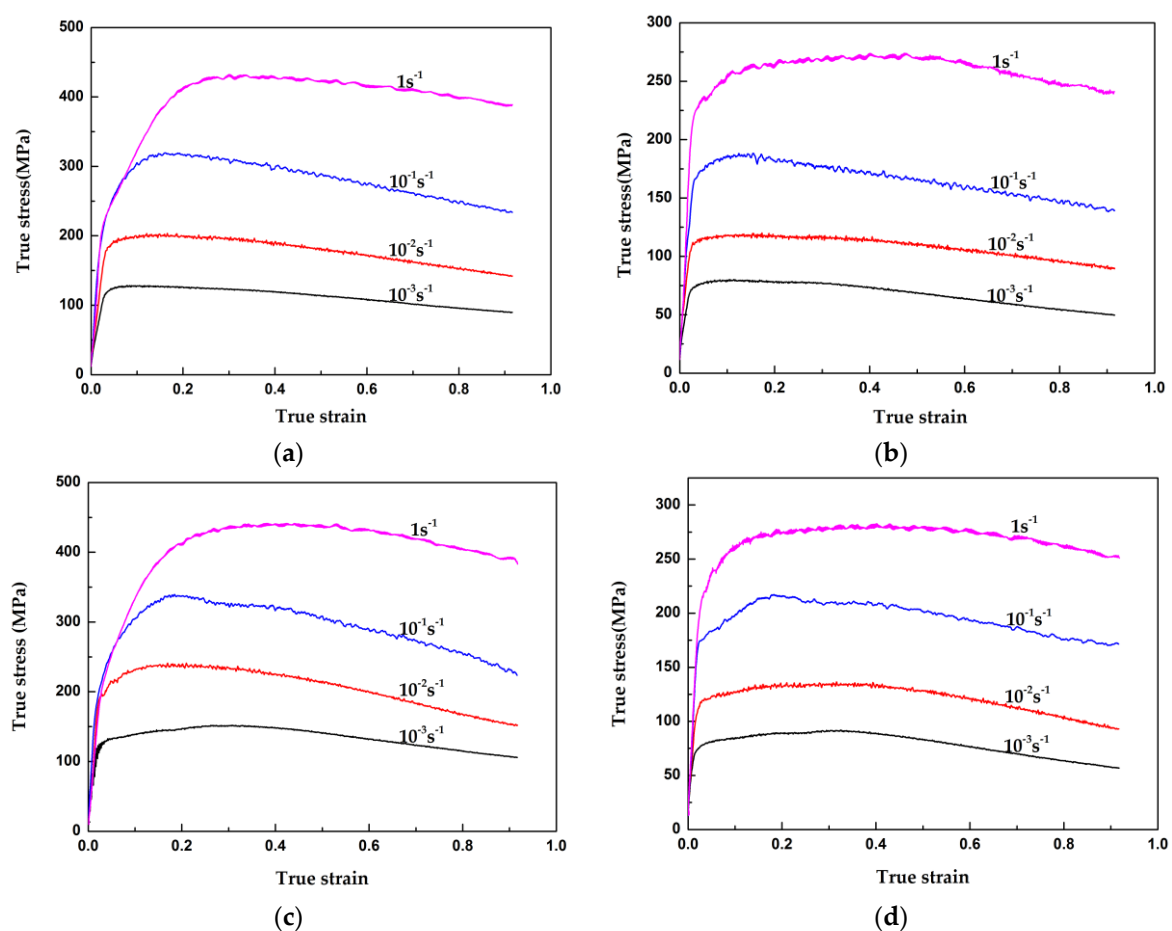


**Figure 3.** True stress–true strain plots at different strain rates and deformation temperature of (a) 900 °C and (b) 1000 °C for the as-cast state and (c) 900 °C and (d) 1000 °C for the homogenized state  $\text{Al}_{0.5}\text{CoCrFeNi}$  HEAs.

In consideration of the influence of homogenization, it is important to note that, in this study, both the peak stress and the steady stress at the homogenized state are higher compared with the as-cast state under the same deformation conditions. However, the increase in flow stress is not very significant since it was almost limited within 30 MPa, as shown in Table 2. This phenomenon can be explained by the following three factors. Firstly, as mentioned above, a large amount of precipitation separated from the matrix during homogenization. They locked the dislocation and grain boundary

during deformation. Secondly, some of the ID regions redissolved to the matrix. On the one hand, this led to a higher degree of solid solution. Since HEAs are considered solid solution alloys and each element can be considered solute atoms [24], the effect of the solid solution strengthening plays a part in the increase in flow stress. On the other hand, the dissolution of ID regions reduced the volume fraction of the BCC phase, which weakened the strength of the samples to some extent. Lastly, the matrix became soft at an elevated temperature and offset the strength effect of the precipitation. This feature is consistent with the findings of a previous study [13]. From the above, it is not difficult to understand the minor increase in flow stress after homogenization.

**Table 2.** The steady state flow stress  $\sigma_{ss}$  ( $\epsilon = 0.8$ ) of the as-cast and homogenized alloys at 900 and 1000 °C with strain rates of  $10^{-3}$ – $1 \text{ s}^{-1}$ .

Temperature (°C)	900				1000				
	$\dot{\epsilon}$ ( $\text{s}^{-1}$ )	$10^{-3}$	$10^{-2}$	$10^{-1}$	1	$10^{-3}$	$10^{-2}$	$10^{-1}$	1
As-cast (MPa)	94	152	247	397	55	95	146	246	246
Homogenized (MPa)	115	168	254	404	63	102	175	263	263

### 3.3. Constitutive Modeling

The interrelation of flow stress ( $\sigma$ ), strain ( $\epsilon$ ), strain rate ( $\dot{\epsilon}$ ), and temperature (T) has been illustrated using constitutive equations derived by several models [25–27]. The Arrhenius model is mostly used because the effect of strain rate and temperature are well considered [28]. In this section, we take the homogenized  $\text{Al}_{0.5}\text{CoCrFeNi}$  HEA as an example. The flow stress and deformation parameters can be expressed as

$$\dot{\epsilon} = A[\sinh(\alpha\sigma)]^n \exp\left(-\frac{Q}{RT}\right) \quad (1)$$

where  $Q$  is activation energy,  $n$  is the stress exponent,  $A$  and  $\alpha$  are experimentally determined constants,  $R$  is gas constant ( $8.3145 \text{ J}/(\text{K}\cdot\text{mol})$ ), and  $T$  is temperature in Kelvin. Taking the logarithm of both sides of Equation (1) yields

$$\ln \dot{\epsilon} = \ln A + n \ln \sinh(\alpha\sigma) - \frac{Q}{RT} \quad (2)$$

$[\sinh(\alpha\sigma)]^n$  can be expressed as follows:

$$[\sinh(\alpha\sigma)]^n = \begin{cases} \sigma^n & \alpha\sigma < 0.8 \\ \exp(\beta\sigma) & \alpha\sigma > 1.2 \end{cases} \quad (3)$$

where  $\alpha$ ,  $\beta$ , and  $n$  are all material constants and

$$\alpha = \beta/n \quad (4)$$

Combining Equations (1), (3), and (4), we get Equations (5) and (6):

$$\dot{\epsilon} = A_1 \sigma^n \exp\left[-\frac{Q}{RT}\right] \quad (5)$$

$$\dot{\epsilon} = A_2 \exp(\beta\sigma) \exp\left[-\frac{Q}{RT}\right] \quad (6)$$

Taking the logarithm of both sides of Equations (5) and (6) yields

$$\ln \dot{\epsilon} = \ln A_1 + n \ln \sigma - \frac{Q}{RT} \quad (7)$$

$$\ln \dot{\epsilon} = \ln A_2 + \beta \sigma - \frac{Q}{RT} \quad (8)$$

The value of  $\beta$  and  $n$  can be obtained from Equations (7) and (8) when the flow stress ( $\sigma$ ) and corresponding strain rate ( $\dot{\epsilon}$ ) are known. Figure 4 shows the relationship of  $\ln\sigma$ – $\ln \dot{\epsilon}$  and  $\sigma$ – $\ln \dot{\epsilon}$  at different deformation temperature, and the lines are obtained by linear fitted through the discrete points. It is important to note, from Figure 3,  $\sigma$  is the symbol for the flow stress at  $\epsilon = 0.8$ , which is in the steady stage of the flow curve. In order to improve the accuracy of the constitutive equation, the curve of  $\dot{\epsilon} = 1 \text{ s}^{-1}$  is not taken in consideration in this section. From the above analysis, the reciprocal of the slope of the lines in Figure 4a,b gives the values of  $n$  and  $\beta$  at particular T. By using average values of  $n$  and  $\beta$  at different T values,  $\alpha$  for  $\epsilon = 0.8$  is calculated as 0.006615.

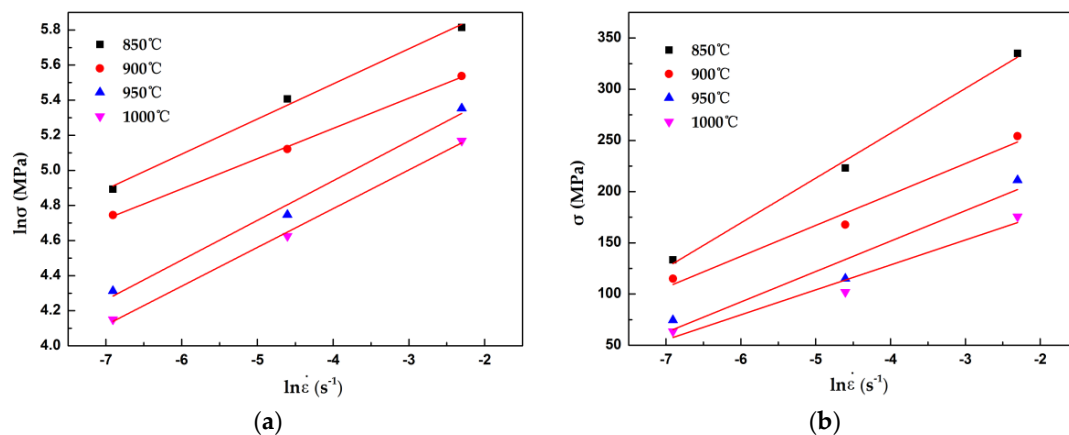


**Figure 4.** Plot of (a)  $\ln\sigma$ – $\ln \dot{\epsilon}$  and (b)  $\sigma$ – $\ln \dot{\epsilon}$  for calculating  $\beta$  and  $n$  at different deformation temperatures. It is important to note that flow stress is taken at  $\epsilon = 0.8$ .

In order to get the activation energy  $Q$ , which indicates plastic deformability, the partial differential equation of Equation (2) is obtained:

$$Q = R \left\{ \frac{\partial \ln \dot{\epsilon}}{\partial \ln [\sinh(\alpha\sigma)]} \right\}_T \left\{ \frac{\partial \ln [\sinh(\alpha\sigma)]}{\partial (1/T)} \right\}_{\dot{\epsilon}} \quad (9)$$

Figure 5 shows the relationship of  $\ln[\sinh(\alpha\sigma)]$ – $\ln \dot{\epsilon}$  at different deformation temperatures and  $\ln[\sinh(\alpha\sigma)]$ – $1/T$  at different strain rates. The first term on the right side of Equation (9) refers to the reciprocal of slopes of the lines in Figure 5a, whereas the second term refers to the slopes of the lines in Figure 5b. By calculation, the average value of  $Q$  of the homogenized  $\text{Al}_{0.5}\text{CoCrFeNi}$  HEA at  $\epsilon = 0.8$  is around 300.99 kJ/mol. As is known,  $Q$  is an important physical parameter indicating the deformation difficulty degree during plastic deformation. The activation energy calculated in this paper is similar to  $\text{CoCuFeNiTi}$  (~316 kJ/mol) [24] and  $\text{AlCrCuNiFeCo}$  (~306 kJ/mol) [28] HEAs reported previously. The influence of temperature and strain rate on hot deformation behavior can be described by Zener-Holloman parameter,  $Z$  [29]:

$$Z = \dot{\epsilon} \exp\left(\frac{Q}{RT}\right) \quad (10)$$

By introducing Equations (10) into (1), another form of the Zener-Holloman parameter is yielded:

$$Z = A [\sinh(\alpha\sigma)]^n \quad (11)$$

Taking the logarithm of both sides of Equation (10) yields

$$\ln Z = \ln A + n \ln [\sinh(\alpha\sigma)] \quad (12)$$

Figure 6 is  $\ln[\sinh(\alpha\sigma)]$  plot versus  $\ln Z$ . The slope and the Y-intercept give the values of  $n$  and  $\ln A$ , relatively. At  $\epsilon = 0.8$ ,  $\ln A = 24.5059$  and  $n = 6.0530$ . Based on the analysis above, a constitutive equation that describes the flow stress of the homogenized  $\text{Al}_{0.5}\text{CoCrFeNi}$  HEA as a function of  $\dot{\epsilon}$  and  $T$  at  $\epsilon = 0.8$  can be written as

$$\dot{\epsilon} = e^{24.5059} [\sinh(0.006615\sigma)]^{6.0530} \exp[-300.99 \times 10^3 / (RT)] \tag{13}$$

Following the similar way, the constitutive equation of as-cast  $\text{Al}_{0.5}\text{CoCrFeNi}$  HEA is derived as Equation (14):

$$\dot{\epsilon} = e^{23.6154} [\sinh(0.006615\sigma)]^{7.1960} \exp[-293.83 \times 10^3 / (RT)] \tag{14}$$

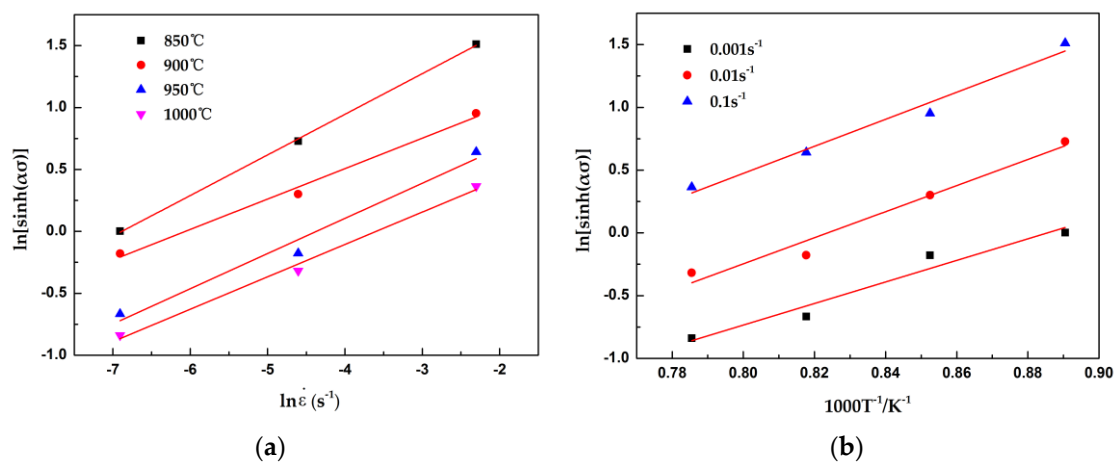


Figure 5. Plot of (a)  $\ln[\sinh(\alpha\sigma)] - \ln \dot{\epsilon}$  at different deformation temperatures and (b)  $\ln[\sinh(\alpha\sigma)] - 1/T$  at different strain rates. It is important to note that the flow stress is taken at  $\epsilon = 0.8$ .

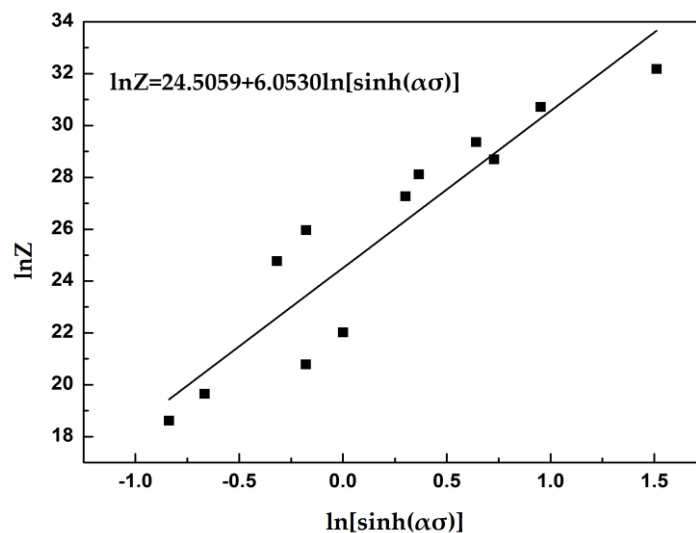


Figure 6. Plot of  $\ln Z - \ln[\sinh(\alpha\sigma)]$ .

### 3.4. Generation of Processing Maps

The hot deformation processing map for the  $\text{Al}_{0.5}\text{CoCrFeNi}$  HEA can be developed on the basis of the dynamic material model (DDM) proposed by Prasad et al [30]. This model assumes that the plastic flow during hot working is a dynamic, nonlinear, and irreversible phenomenon [31]. It considers hot working as a dissipater of power, and the instantaneous power dissipates at a given strain rate ( $\dot{\epsilon}$ )

consists of two complementary parts: temperature rise and microstructural transition. The former is called dissipater content  $G$ , and the latter is called dissipater co-content  $J$ . Moreover, the strain rate sensitivity ( $m$ ) is used to partition  $G$  and  $J$  [32]:

$$m = \frac{dJ}{dG} = \frac{\dot{\epsilon} d\sigma}{\sigma d\dot{\epsilon}} = \frac{\partial(\ln \sigma)}{\partial(\ln \dot{\epsilon})} \quad (15)$$

For an ideal liner power dissipater,  $m = 1$  and  $J_{\max} = \sigma \dot{\epsilon} / 2$ . The efficiency of power dissipation is given by the dimensionless parameter,  $\eta$  [33], as

$$\eta = \frac{J}{J_{\max}} = \frac{2m}{2m + 1} \quad (16)$$

The power dissipation map can be obtained by plotting the iso-efficiency contour lines of  $\eta$  on the temperature–strain rate field. The value of  $\eta$  represents the way in which material dissipates power through different metallurgical processes such as dynamic recovery, dynamic recrystallization, flow localization, and superplasticity. The higher the  $\eta$  value is, the more the amount of power dissipated by the microstructure changes increases. Generally, in many of the metallic alloys, it has been reported that a higher peak  $\eta$  leads to a better workability of the materials [34]. However, flow localization such as shear band can also have higher efficiency, which is not ideal for thermo-mechanical processing. Therefore, the condition for instability should be taken into account [30].

$$\xi(\dot{\epsilon}) = \frac{\partial \ln\left(\frac{m}{m+1}\right)}{\partial \ln \dot{\epsilon}} + m < 0 \quad (17)$$

where  $\xi(\dot{\epsilon})$  is a dimensionless instability parameter, and the variation of  $\xi(\dot{\epsilon})$  with temperature and strain rate constitutes an instability map. In this map, domains with negative values of  $\xi(\dot{\epsilon})$  indicate flow instability. Combining the instability map with the power dissipation map, we can obtain the processing map.

Based on the above theory, the processing maps of the as-cast and homogenized  $\text{Al}_{0.5}\text{CoCrFeNi}$  HEAs at the true strain of 0.8 are shown in Figure 7. The isolines represent the constant efficiency of power dissipation, while the red areas (Domain A) represent the instability domains ( $\xi(\dot{\epsilon}) < 0$ ). From Figure 7, we can obtain an obvious tendency that the efficiency of power dissipation increases with increasing deformation temperatures and decreasing strain rate, which is to say that the value of  $\eta$  keeps increasing from the upper-left corner to the lower-right corner, as the blue dashed line indicates if we temporarily ignore Domain C in Figure 7b. The climbing of the edge dislocation and the crossing sliding of the screw dislocation accelerate at a higher temperature, and a lower strain rate can provide more time to accumulate the dislocation density. Therefore, a higher temperature and a lower strain rate are beneficial for a microstructure transition, such as dynamic recovery and recrystallization, during hot deformation, which can enlarge the value of  $\eta$  [35]. On the contrary, a lower temperature and a higher strain rate usually lead to flow instabilities because of the formation of adiabatic shear bands, dynamic strain aging, mechanical twinning, and flow rotations [36]. Therefore, the instability domain is found in the upper-left corner of the maps, which is 850–870 °C and  $10^{-1.3}$ – $10^{-0.2}$  s<sup>-1</sup> for the as-cast state and 850–865 °C and  $10^{-1.3}$ – $10^{-0.3}$  s<sup>-1</sup> for the homogenized state.

The difference in Figure 7a,b can be explained by the fact that the peak value of  $\eta$  is 0.4 and appears in the region of 990–1000 °C and  $10^{-3}$ – $10^{-2.4}$  s<sup>-1</sup> for the as-cast state while it is 0.42 and appears in the region of 945–965 °C and  $10^{-1.7}$ – $10^{-1.1}$  s<sup>-1</sup> for the homogenized state. It should be emphasized that a relatively lower deformation temperature and a higher strain rate is easier to be achieved in practice. Some previous reports about aluminium alloys have confirmed that the homogenized state has a higher degree of dynamic recrystallization when compared with the as-cast state under the same hot deformation [37,38]. This may be explained by the migration of the peak region of  $\eta$  in Figure 7b. As we all know, the microstructure evolution of alloys after a certain degree of plastic deformation

consists of three stages: dynamic recovery, dynamic recrystallization, and grain growth. A rising holding time and an increasing temperature can accelerate the growth of recrystallized grain and even generate coarse grains, which would worsen the processability. Therefore, coarse grains may be generated in Domain C of Figure 7b and prevent any increase in the value of  $\eta$ . However, it should be noted that research about microstructure evolution during hot deformation is vital in the future in order to clarify the mechanism of the dynamic recrystallization of  $\text{Al}_{0.5}\text{CoCrFeNi}$  HEAs.

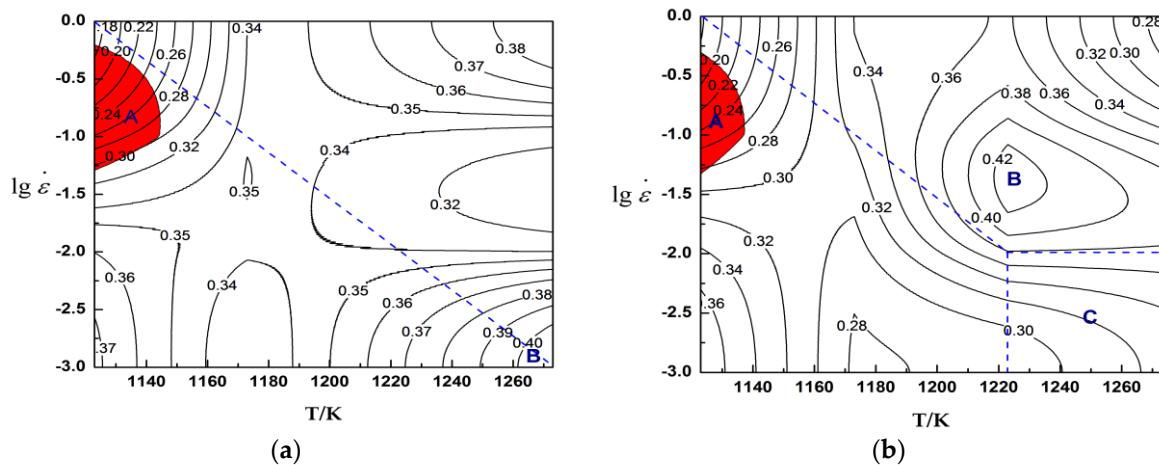


**Figure 7.** Processing maps of the (a) as-cast and (b) homogenized state  $\text{Al}_{0.5}\text{CoCrFeNi}$  high entropy alloys (HEAs) at a true strain state of 0.8. A, B and C correspond to different regions. (A—instability regions, B—optimum thermo-mechanical processing regions, C—high temperature and low strain rate region of (b)).

#### 4. Conclusions

The hot working characteristics of the  $\text{Al}_{0.5}\text{CoCrFeNi}$  HEA were investigated through compression testing in a Gleeble-3500 thermo-mechanical simulator in the temperature range of 850–1000 °C with a strain rate range of  $10^{-3}$ – $1 \text{ s}^{-1}$ . Based on the results and discussion above, the following conclusions can be drawn:

- (1) The flow behavior of  $\text{Al}_{0.5}\text{CoCrFeNi}$  HEA is sensitive to deformation temperature and strain rate. The flow stress increases with the increase in strain rate and the decrease in deformation temperature. Moreover, the homogenized alloy shows a higher flow stress compared with the as-cast alloy under the same deformation condition.
- (2) The average activation energy of the as-cast and homogenized  $\text{Al}_{0.5}\text{CoCrFeNi}$  alloys is calculated to be 293.83 and 300.99 kJ/mol, respectively. The constitutive equation that describes the flow stress of the homogenized  $\text{Al}_{0.5}\text{CoCrFeNi}$  alloy as a function of strain rate and deformation temperature at a true strain of 0.8 was determined to be

$$\dot{\varepsilon} = e^{24.5059} [\sinh(0.006615\sigma)]^{6.0530} \exp[-300.99 \times 10^3 / (RT)]$$

- (3) Processing maps show that the homogenized alloy has a better hot workability than as-cast alloy because the optimum thermo-mechanical processing parameters are relatively easier to determine. The optimum processing parameters of the homogenized  $\text{Al}_{0.5}\text{CoCrFeNi}$  HEA are  $T = 945$ – $965$  °C and strain rate  $\dot{\varepsilon} = 10^{-1.7}$ – $10^{-1.1} \text{ s}^{-1}$ .

**Supplementary Materials:** The following are available online at [www.mdpi.com/2075-4701/6/11/277/s1](http://www.mdpi.com/2075-4701/6/11/277/s1). Figure S1: (a) The thermal expansivity curve with temperature (black color) and its differential curve (blue color) of as-cast  $\text{Al}_{0.5}\text{CoCrFeNi}$  HEA at a heating rate of 5 °C/min. (b) Partial enlargement drawing of the thermal expansivity curve at  $T = 810$ – $870$  °C.

**Acknowledgments:** This study was financially supported by the National Natural Science Foundation of China (Grant No. 51571161 and 51271151), the Natural Science Basic Research Plan in Shaanxi Province of China (2013JQ5003), and the Program of Introducing Talents of Discipline to Universities (Grant No. B08040).

**Author Contributions:** Jinshan Li and Jun Wang conceived and designed the experiments; Yu Zhang and Sizhe Niu performed the experiments; Jun Wang and Yu Zhang analyzed the data; Hongchao Kou contributed reagents/materials/analysis tools; Yu Zhang wrote the paper.

**Conflicts of Interest:** The authors declare no conflict of interest.

## References

1. Kumar, N.A.P.K.; Li, C.; Leonard, K.J.; Bei, H.; Zinkle, S.J. Microstructural stability and mechanical behavior of FeNiMnCr high entropy alloy under ion irradiation. *Acta Mater.* **2016**, *113*, 230–244. [[CrossRef](#)]
2. Troparevsky, M.C.; Morris, J.R.; Daene, M.; Wang, Y.; Lupini, A.R.; Stocks, G.M. Beyond Atomic Sizes and Hume-Rothery Rules: Understanding and Predicting High-Entropy Alloys. *J. Miner. Met. Mater. Soc.* **2015**, *67*, 2350–2363. [[CrossRef](#)]
3. Yeh, J.W.; Chen, S.K.; Lin, S.J.; Gan, J.Y.; Chin, T.S.; Shun, T.T.; Tsau, C.H.; Chang, S.Y. Nanostructured High-Entropy Alloys with Multiple Principal Elements: Novel Alloy Design Concepts and Outcomes. *Adv. Eng. Mater.* **2004**, *6*, 299–303. [[CrossRef](#)]
4. Zhang, Y.; Zuo, T.T.; Tang, Z.; Gao, M.C.; Dahmen, K.A.; Liaw, P.K.; Lu, Z.P. Microstructures and properties of high-entropy alloys. *Prog. Mater. Sci.* **2014**, *61*, 1–93. [[CrossRef](#)]
5. Gali, A.; George, E.P. Tensile properties of high- and medium-entropy alloys. *Intermetallics* **2013**, *39*, 74–78. [[CrossRef](#)]
6. Otto, F.; Dlouhý, A.; Somsen, C.; Bei, H.; Eggeler, G.; George, E.P. The influences of temperature and microstructure on the tensile properties of a CoCrFeMnNi high-entropy alloy. *Acta Mater.* **2013**, *61*, 5743–5755. [[CrossRef](#)]
7. Sriharitha, R.; Murty, B.S.; Kottada, R.S. Alloying, thermal stability and strengthening in spark plasma sintered Al<sub>x</sub>CoCrCuFeNi high entropy alloys. *J. Alloy. Compd.* **2014**, *583*, 419–426. [[CrossRef](#)]
8. Zhang, Y.; Stocks, G.M.; Jin, K.; Lu, C.; Bei, H.; Sales, B.C.; Wang, L.; Béland, L.K.; Stoller, R.E.; Samolyuk, G.D. Influence of chemical disorder on energy dissipation and defect evolution in concentrated solid solution alloys. *Nat. Commun.* **2015**, *6*, 8736. [[CrossRef](#)] [[PubMed](#)]
9. Kuznetsov, A.V.; Shaysultanov, D.G.; Stepanov, N.D.; Salishchev, G.A.; Senkov, O.N. Tensile properties of an AlCrCuNiFeCo high-entropy alloy in as-cast and wrought conditions. *Mater. Sci. Eng. A* **2012**, *533*, 107–118. [[CrossRef](#)]
10. Wang, W.R.; Wang, W.L.; Wang, S.C.; Tsai, Y.C.; Lai, C.H.; Yeh, J.W. Effects of Al addition on the microstructure and mechanical property of Al<sub>x</sub>CoCrFeNi high-entropy alloys. *Intermetallics* **2012**, *26*, 44–51. [[CrossRef](#)]
11. Shun, T.T.; Du, Y.C. Microstructure and tensile behaviors of FCC Al<sub>0.3</sub>CoCrFeNi high entropy alloy. *J. Alloy. Compd.* **2009**, *479*, 157–160. [[CrossRef](#)]
12. Tian, F.; Varga, L.K.; Chen, N.; Shen, J.; Vitos, L. Empirical design of single phase high-entropy alloys with high hardness. *Intermetallics* **2015**, *58*, 1–6. [[CrossRef](#)]
13. Lin, C.M. Evolution of microstructure, hardness, and corrosion properties of Al<sub>0.5</sub>CoCrFeNi high-entropy alloy. *Intermetallics* **2011**, *19*, 288–294. [[CrossRef](#)]
14. Lu, Y.; Dong, Y.; Guo, S.; Jiang, L.; Kang, H.; Wang, T.; Wen, B.; Wang, Z.; Jie, J.; Cao, Z. A promising new class of high-temperature alloys: Eutectic high-entropy alloys. *Sci. Rep.* **2014**, *4*, 6200. [[CrossRef](#)] [[PubMed](#)]
15. Wang, W.R.; Wang, W.L.; Yeh, J.W. Phases, microstructure and mechanical properties of Al<sub>x</sub>CoCrFeNi high-entropy alloys at elevated temperatures. *J. Alloy. Compd.* **2014**, *589*, 143–152. [[CrossRef](#)]
16. Gludovatz, B.; Hohenwarter, A.; Catoor, D.; Chang, E.H.; George, E.P.; Ritchie, R.O. A fracture-resistant high-entropy alloy for cryogenic applications. *Science* **2014**, *345*, 1153–1158. [[CrossRef](#)] [[PubMed](#)]
17. Tsai, C.H. Factor analysis of the clustering of common somatic symptoms: A preliminary study. *BMC Health Serv. Res.* **2010**, *10*, 1–8. [[CrossRef](#)] [[PubMed](#)]
18. Li, C. Effect of aluminum contents on microstructure and properties of Al<sub>x</sub>CoCrFeNi alloys. *J. Alloy. Compd.* **2010**, *504*, S515–S518. [[CrossRef](#)]

19. Salishchev, G.A.; Tikhonovsky, M.A.; Shaysultanov, D.G.; Stepanov, N.D.; Kuznetsov, A.V.; Kolodiy, I.V.; Tortika, A.S.; Senkov, O.N. Effect of Mn and V on structure and mechanical properties of high-entropy alloys based on CoCrFeNi system. *J. Alloy. Compd.* **2014**, *591*, 11–21. [[CrossRef](#)]
20. Stepanov, N.D.; Shaysultanov, D.G.; Yurchenko, N.Y.; Zharebtsov, S.V.; Ladygin, A.N.; Salishchev, G.A.; Tikhonovsky, M.A. High temperature deformation behavior and dynamic recrystallization in CoCrFeNiMn high entropy alloy. *Mater. Sci. Eng. A* **2015**, *636*, 188–195. [[CrossRef](#)]
21. Tang, Z.; Gao, M.C.; Diao, H.; Yang, T.; Liu, J.; Zuo, T.; Zhang, Y.; Lu, Z.; Cheng, Y.; Zhang, Y. Aluminum Alloying Effects on Lattice Types, Microstructures, and Mechanical Behavior of High-Entropy Alloys Systems. *J. Miner. Met. Mater. Soc.* **2013**, *65*, 1848–1858. [[CrossRef](#)]
22. Li, B.; Pan, Q.; Yin, Z. Characterization of hot deformation behavior of as-homogenized Al–Cu–Li–Sc–Zr alloy using processing maps. *Mater. Sci. Eng. A* **2014**, *614*, 199–206. [[CrossRef](#)]
23. Zhang, Y.; Jiang, S.; Zhao, Y.; Shan, D. Isothermal precision forging of complex-shape rotating disk of aluminum alloy based on processing map and digitized technology. *Mater. Sci. Eng. A* **2013**, *580*, 294–304. [[CrossRef](#)]
24. Samal, S.; Rahul, M.R.; Kottada, R.S.; Phanikumar, G. Hot deformation behaviour and processing map of Co-Cu-Fe-Ni-Ti eutectic high entropy alloy. *Mater. Sci. Eng. A* **2016**, *664*, 227–235. [[CrossRef](#)]
25. Shi, H.; McLaren, A.J.; Sellars, C.M.; Shahani, R.; Bolingbroke, R. Constitutive equations for high temperature flow stress of aluminium alloys. *Mater. Sci. Technol.* **2013**, *13*, 210–216. [[CrossRef](#)]
26. Zhou, M.; Clode, M.P. Modelling of high temperature viscoplastic flow of aluminium alloys by hot torsion testing. *Mater. Sci. Technol.* **1997**, *13*, 818–824. [[CrossRef](#)]
27. Sheppard, T.; Jackson, A. Constitutive equations for use in prediction of flow stress during extrusion of aluminium alloys. *Mater. Sci. Technol.* **1997**, *13*, 203–209. [[CrossRef](#)]
28. Nayan, N.; Singh, G.; Murty, S.V.S.N.; Jha, A.K.; Pant, B.; George, K.M.; Ramamurty, U. Hot deformation behaviour and microstructure control in AlCrCuNiFeCo high entropy alloy. *Intermetallics* **2014**, *55*, 145–153. [[CrossRef](#)]
29. Zener, C.; Hollomon, J.H. Effect of Strain Rate upon Plastic Flow of Steel. *J. Appl. Phys.* **1944**, *15*, 22–32. [[CrossRef](#)]
30. Prasad, Y.V.R.K.; Gegel, H.L.; Doraivelu, S.M.; Malas, J.C.; Morgan, J.T.; Lark, K.A.; Barker, D.R. Modeling of dynamic material behavior in hot deformation: Forging of Ti6242. *Metall. Mater. Trans. A* **1984**, *15*, 1883–1892. [[CrossRef](#)]
31. Prasad, Y.V.R.K.; Rao, K.P. Processing maps and rate controlling mechanisms of hot deformation of electrolytic tough pitch copper in the temperature range 300–950 °C. *Mater. Sci. Eng. A* **2005**, *391*, 141–150. [[CrossRef](#)]
32. Prasad, Y.V.R.K.; Seshacharyulu, T. Processing maps for hot working of titanium alloys. *Mater. Sci. Eng. A* **1998**, *243*, 82–88. [[CrossRef](#)]
33. Prasad, Y.V.R.K.; Seshacharyulu, T. Modelling of hot deformation for microstructural control. *Int. Mater. Rev.* **1997**, *43*, 243–258. [[CrossRef](#)]
34. Prasad, Y.V.R.K.; Rao, K.P.; Sasidhara, S. *Hot Working Guide: A Compendium of Processing Maps*; ASM International: Geauga County, OH, USA, 2015; pp. 188–195.
35. Yang, Y.; Zhang, Z.; Zhang, X. Processing map of Al<sub>2</sub>O<sub>3</sub> particulate reinforced Al alloy matrix composites. *Mater. Sci. Eng. A* **2012**, *558*, 112–118. [[CrossRef](#)]
36. Lin, Y.C.; Li, L.T.; Xia, Y.C.; Jiang, Y.Q. Hot deformation and processing map of a typical Al–Zn–Mg–Cu alloy. *J. Alloy. Compd.* **2013**, *550*, 438–445. [[CrossRef](#)]
37. Chen, L.; Zhao, G.; Gong, J.; Chen, X.; Chen, M. Hot Deformation Behaviors and Processing Maps of 2024 Aluminum Alloy in As-cast and Homogenized States. *J. Mater. Eng. Perform.* **2015**, *24*, 5002–5012. [[CrossRef](#)]
38. Hakamada, M.; Watazu, A.; Saito, N.; Iwasaki, H. Effects of Homogenization Annealing on Dynamic Recrystallization in Mg–Al–Ca–RE (Rare Earth) Alloy. *Mater. Trans.* **2008**, *49*, 1032–1037. [[CrossRef](#)]

